GUVI Ground Calibration Report

Version 1.1

Applied Physics Laboratory
Laurel, MD 20723-6099

Version 1.0 - December 2001
D. C. Humm

Version 1.1 - November 2007
B.C. Wolven

TABLE OF CONTENTS

FIGURES

TABLES

1. INTRODUCTION

1.1. Objectives

This document describes the calibration of the GUVI instrument. The principal objective of characterization is the accurate conversion of a sensor signal to a source radiance or aperture irradiance on a per pixel basis. For the GUVI spectrographic imager, calibration algorithms will convert signal to spectral radiance or spectral irradiance. Instrument characterization permits an understanding of in-flight performance, while documentation ensures that future instruments may profit from the GUVI experience. Data analysis activities are often frustrated by an inadequate knowledge of the instruments characteristics. This plan seeks to avoid many of these problems by providing the information that may serve to resolve future issues concerning the data reduction and analysis procedures for the GUVI data.

The GUVI instrument was calibrated on the ground using facilities that had been built for the MSX program and the calibration of the UVISI instruments. The techniques and procedures are based on those developed for the SSUSI program. Ground calibration of GUVI will make use of the APL facilities but also, as a cross calibration, may use other facilities for additional or component characterization. In-flight calibrations are a vital part of the instrument lifecycle and will occur throughout the mission. The results of in-flight calibration measurements are described in the *GUVI Stellar Calibration Procedure* document.

The ground calibration of GUVI occupied a central portion of the pre-launch preparations. Ground calibrations may be broken down into several levels. The sub-component level calibrations involved tests of the individual focal plane units (FPUs) . The component level calibrations involved tests of the assembled FPUs and associated optical units. Finally, the system level calibrations consisted of full-up or "end-to-end" tests of the entire instrument with all of the components operating.

GUVI is an important element in the NASA TIMED mission’s investigation of the physical and chemical processes in the Earth's upper atmosphere (above 80 km). The upper atmosphere is the region that contains the mesophere, thermosphere, and ionosphere. This region is poorly understood due to the difficulty in carrying out in situ measurements, its inherent complexity, and the need to develop a comprehensive global picture of this environment. While the basic physics that controls this region is understood, it does represent a difficult region to

model since the atmospheric temperature and temperature gradients reach their largest values, composition changes from molecular to predominantly atomic, complex chemical and electrodynamic processes become the major determinants of composition, and where the combination of these effects prevent an adequate global description of the upper atmospheric "weather".

The study of the upper atmosphere has witnessed a major change in the last decade as ultraviolet technology has made the transition from spectroscopy to remote sensing. Traditionally the concern of optical aeronomers (scientists who study the structure, composition, and dynamics of the upper atmosphere using optical means) had been the identification of the excitation and emission mechanisms of spectral features. With the advent of an adequate physical description of the phenomena it has become possible to move beyond the simple identification of features to their interpretation in terms of geophysical parameters.

The FUV is ideally suited to determining thermospheric and ionospheric environmental parameters. It possesses optical signatures of all the major thermospheric species O, N_2, and O_2 (O_2 is seen in absorption on the limb) and the dominant F-region ion, O^+ (on the nightside). Since we understand the processes which produce this radiation, we know that we need not telemeter down the entire FUV spectrum but can identify a few wavelength bands or "colors" that provide all the information required for an unambiguous determination of these environmental parameters.

1.2. Instrument Description

GUVI consists of two separate modules: a scanning imaging spectrograph (SIS) and the Support Electronics Module (SEM). The normal mode for the SIS is to scan from horizon-to-horizon as shown schematically in Figure 1. It can also operate in the "spectrograph" mode where the scan angle is held fixed and the entire spectrum is downlinked (N.B. because of bandwidth limitations only five spectral regions called "colors" can be downlinked in the imaging mode).

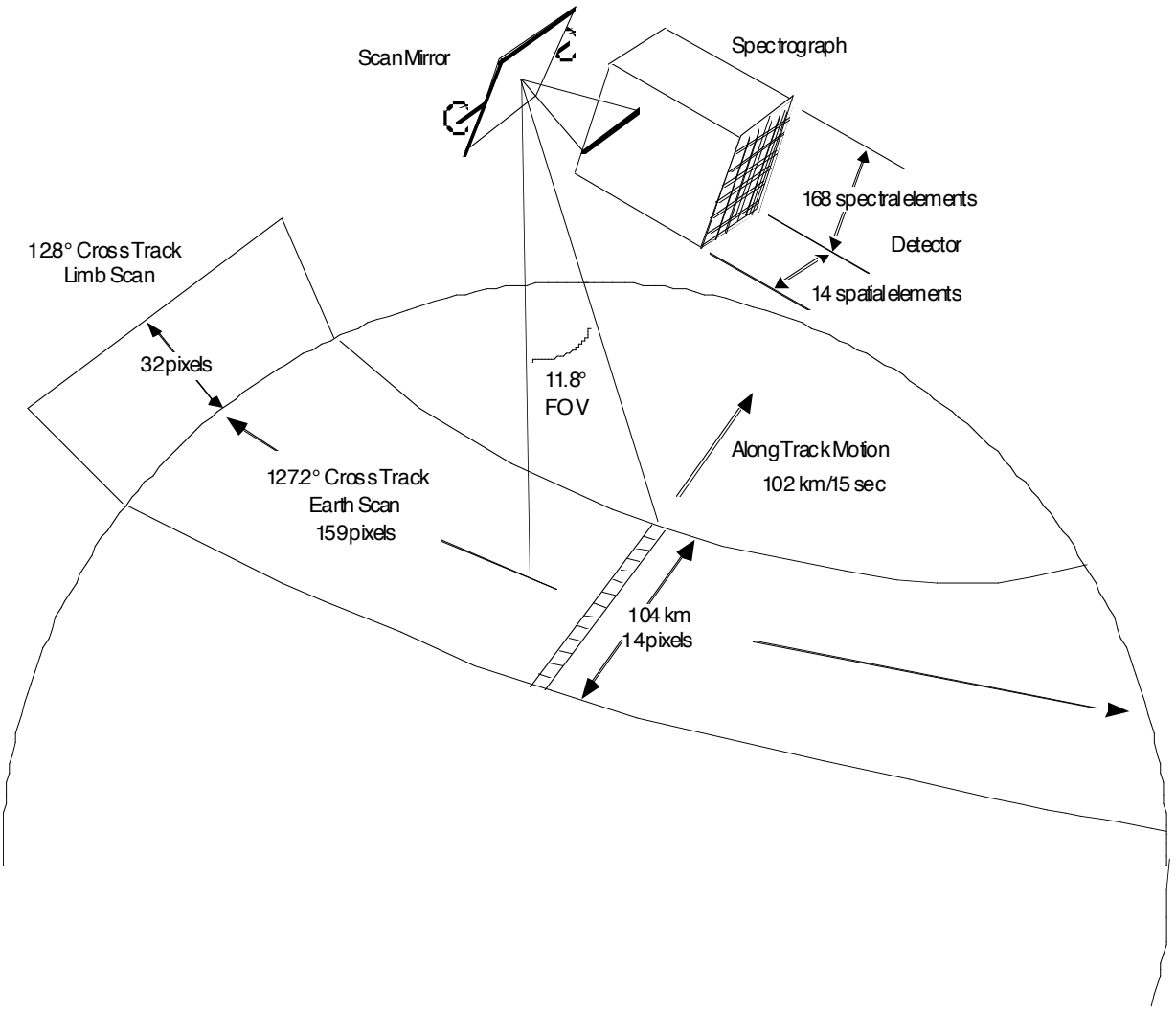

Figure 1. SIS scanning geometry.

The GUVI sensor contains a line scanning imaging spectrograph covering the far ultraviolet spectrum which has two modes of operation. The imaging mode produces horizon to horizon line scan images at five simultaneous far ultraviolet wavelengths. In the spectrograph mode, the entire far ultraviolet spectrum is downlinked at one selected look angle.

A block diagram of GUVI is shown in Figure 2. The support module contains the processor, control, and power switching circuitry required by the flight unit.

Figure 2. GUVI block diagram.

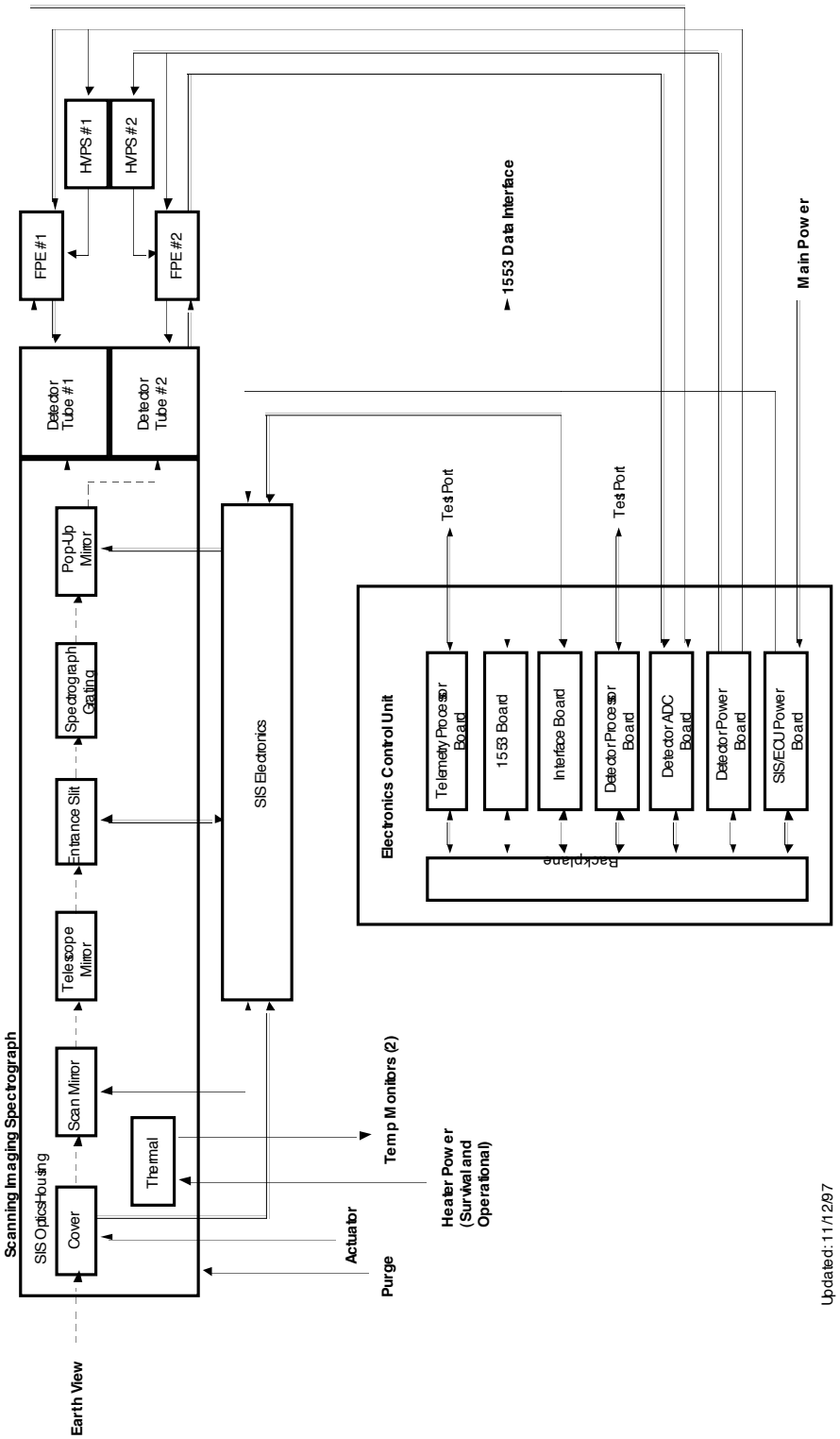

1.2.1. Scanning Imaging Spectrograph (SIS)

The scanning imaging spectrograph (or SIS) consists of a sunshade, a scanning mirror, a slit mechanism, the telescope primary mirror, a toroidal grating, a 2D focal plane assembly, and an electronics package (Figure 2). The primary mirror collects incident light and directs it through a slit. Three slits and a closed position are available. The toroidal grating disperses the light in wavelength and focuses it onto an effective array of 176x14 "pixels" on the focal plane (a position sensitive anode is used so the term "pixels" refers just to the resolution of the binning rather than to the resolution of the detector). The 176 elements represent a spectral dimension perpendicular to the slit, while the 14 elements represent a linear spatial dimension along the slit. Instrument electronics can sum these pixels, thus sampling the spectral dimension in groups of 176 or 5 colors and the spatial dimension in groups of 14 pixels. In conjunction with a particular slit, the instantaneous field of view (IFOV) is scanned in the "imaging" mode by the motion of the scan mirror.

The scanning motion of the primary mirror sweeps the IFOV perpendicular to the long axis of the slit and measures a second spatial dimension orthogonal to the slit's long dimension. This can be at most 140 degrees and is controlled by the GUVI microprocessor. The mirror scans in discrete increments of either 0.4° (that is, the mirror stops scanning within each accumulation interval) so that the instrument can sample an unblurred, spatially contiguous scene of up to 11.8°x.74° anywhere within its 11.8°x140° field of regard (FOR). The mirror can stop at a given angular position in its scan (spectrograph mode).

The imaging spectrograph builds multispectral images by scanning spatially across the satellite track (Figure 1). One dimension of the detector array contains 14 spatial pixels (along the spacecraft track), and the other dimension contains of 176 spectral bins over the range of 120 to 180 nm. The scan mirror sweeps the 14 spatial pixel footprint from horizon to horizon perpendicular to the spacecraft motion, producing one frame of 14 cross-track lines in 15 seconds. Simultaneous image frames are generated over the entire wavelength range in the imaging mode, but the data rate allocation limits the downlinked image data to five different wavelength intervals or “colors.”

The imaging mode scan cycle consists of a limb viewing section followed by an Earth viewing section. Limb viewing pixels are collected from 80° from nadir (the start of scan) to -60° from nadir. The limb viewing section has a cross track resolution of 0.4° per pixel, and consists of 32

cross track pixels by 14 along track pixels at five wavelengths. At 80° from nadir and a spacecraft altitude of 600 km, the spectrograph will view approximately 500 km above the horizon. One should note that the same pixel on the limb is resampled three times on each orbit due to the wide horizontal field-of-view.

In the spectrograph mode, the scan mirror is held at a fixed viewing angle (normally either the nadir direction for "ground truth" or on the limb for star calibrations). The along track dimension of the detector array is binned into 14 spatial pixels. Spectral data from all 168 bins are produced for the 14 spatial pixels every 3.0 seconds (see Table 1). The entire spectrum, consisting of all 176 bins, can be downlinked in the allocated "spare" words in the data stream. The spectrograph mode (in which the entire spectrum is downlinked) would be used predominantly during stellar calibration operations and for "ground truth" campaigns in which we will stare at the radiating volume above a ground site.

The imaging spectrograph contains three entrance slits of varying widths. The intermediate width slit is intended for use during imaging mode operation. The widest slit would be used in imaging mode to increase the sensitivity should the optical efficiency of the system decrease over time or to minimize the statistical error for low count rate scenes such as when the FUV nightglow is to be observed. The narrowest slit improves the spectral resolution. Any slit can be used in any mode of operation. Furthermore, the slit mechanism is designed so that two motors must fail (they are independent) in a specific (i.e. "closed") mode in order for the aperture to be "shuttered". The expected "failure" mode would be one that would leave us with a fixed slit.

Table 1 summarizes the SIS performance characteristics. Note that normally imaging mode uses the 0.30 deg slit and that to reduce the size of the table we have indicated the "normal" slit for the spectrograph mode as being the narrowest (0.18 deg) even though any one of the three slit widths can be used for either of the two modes.

Table 1. GUVI SIS Performance

Parameter/Mode	Full scan, Imaging	Spectrograph
IFOV, cross track, normal	0.30°	0.18°
IFOV, cross track, wide slit	0.74°	--
IFOV, along track	11.84°	11.84°
Pixel FOV (limb), cross track	0.30°	0.18°
Pixel FOV (limb), along track	0.85°	0.85°
Pixel FOV (Earth), cross track	0.30°	0.18°
Pixel FOV (Earth), along track	0.85°	0.85°
Scan FOV (limb), cross track	12.8°	--
Scan FOV (limb), step resolution	0.4°	--
Scan FOV (Earth), cross track	127.2°	--
Scan FOV (Earth), step resolution	0.8°	--
Nadir spatial resolution, cross	7 km	2 km
Nadir spatial resolution, along	7.5 km	7.5 km
Pixel step period (limb)	0.68 sec	--
Pixel step period (Earth)	0.68 sec	--
Spectral resolution, narrow	1.3 nm	1.3 nm
Spectral resolution, normal	2.0 nm	2.0 nm
Spectral resolution, wide	4.2 nm	4.2 nm
Responsivity at 135.6 nm	0.06 c/s/R	--
Responsivity from 140-150 nm	0.21 c/s/R	--
Data Rate	8.105 kbps	8.105 kbps
Data Frame Period	15 sec	3.0 sec
Image size (limb), cross track	32 pixels	1 pixel
Image size (limb), along track	14 pixels	14 pixels
Image size (Earth), cross track	159 pixels	1 pixel
Image size (Earth), along track	14 pixels	14 pixels
Output word size (limb)	8 bits	8 bits
Output word size (Earth)	8 bits	8 bits

The SIS consists of a cross-track scanning mirror at the input to a telescope (a 75 mm focal length off-axis parabola system with a 20 mm x 25 mm clear aperture) and a Rowland circle spectrograph. The SIS is an *f*/3 system with a toroidal grating. The optical path incorporates baffles to prevent stray light from reaching the focal plane at the slit and the detector. The telescope mirror can not see any surfaces, other than baffle knife edges, that are illuminated by sources beyond the entrance opening of the spectrograph. The optical surfaces are coated with ARC Coating #1200 or ARC Coating #1600 to tune the system performance to the observational requirements.

The imaging spectrograph includes two detectors. Either one can be used since the pop-up mirror, which enters the optical path when the second detector is to be used, is retractable. Only one detector is operated at a time. The detector characteristics are listed in Table 2. The use of the secondary detector will lower the sensitivity of the imaging spectrograph due to the extra reflection of the pop-up mirror. The sensitivity with the secondary detector in place will be approximately 75% of the sensitivity with the primary detector since the pop-mirror has the ARC #1200 MgF_2 overcoat. The sensitivities listed in Table 1 are for the primary detector.

The detector consists of a microchannel plate intensifier with a wedge and strip anode. Since maintenance of performance specifications over the mission lifetime is a design driver, the HVPS is commandable so that the detector gain can be maintained at $5x10^6$ even at a charge extraction rate as high as 10 Coulomb/yr.

Table 2. UV Detector Characteristics

Characteristic	Value	Units
Minimum Frame Period	0.034	seconds
Photocathode	CsI	--
Input Window	MgF_2	--
Detector Size (Diameter)	25	mm
MCP Arrangement	Z stack	--
Anode	Wedge & Strip	--
Quantum Efficiency At 135 Nm	10	per cent
Position Resolution, Spatial	14 elements	per 16.5 mm
Position Resolution, Spectral	168 elements	per 15.6 mm
Mean Gain	5×10^6	electrons/photon
Power	3	watts
Weight	4	lbs
Qualification Temperature Range	-29 to +50	C

2. Ground Calibration Facilities

2.1. Introduction

The Optical Calibration Facility at JHU/APL is designed for end-to-end calibration of optical instruments at wavelengths ranging from the FUV to the NIR. In the past five years the Applied Physics Laboratory has built, tested, and calibrated 23 spaceflight-qualified imagers and spectrographs at the OCF. Nine of these were launched on the Midcourse Space Experiment (MSX), two were included on the Near-Earth Asteroid Rendezvous (NEAR) spacecraft, two on the Comet Nucleaus Tour (CONTOUR) mission, five are spectrographs for the Defense Meteorological Satellite Program (DMSP), and five are for the TIMED satellite, including four TIDI telescopes and the GUVI instrument. With each calibration, improvements are made and the facility becomes better characterized.

The OCF has several primary components assembled in a modular fashion. Either a monochromator or integrating sphere provides a light source. A collimator ensures that the beam consists of parallel rays. A target chamber provides a mounting platform on which an instrument can receive the collimated beam. The OCF also includes broadband sources, filters, windows, valves, connector pipes, and calibrated detectors. The entire facility can be pumped down to low pressures that allow the propagation of radiation in the middle and far ultraviolet, and the temperature of the target chamber can be controlled. Most of these various components may be removed, interchanged, or replaced, making the OCF an entirely modular operation. The larger components such as the monochromator and collimator are mounted on carts to facilitate access and rearrangement. Figure 3 shows a schematic diagram of the Optical Calibration Facility.

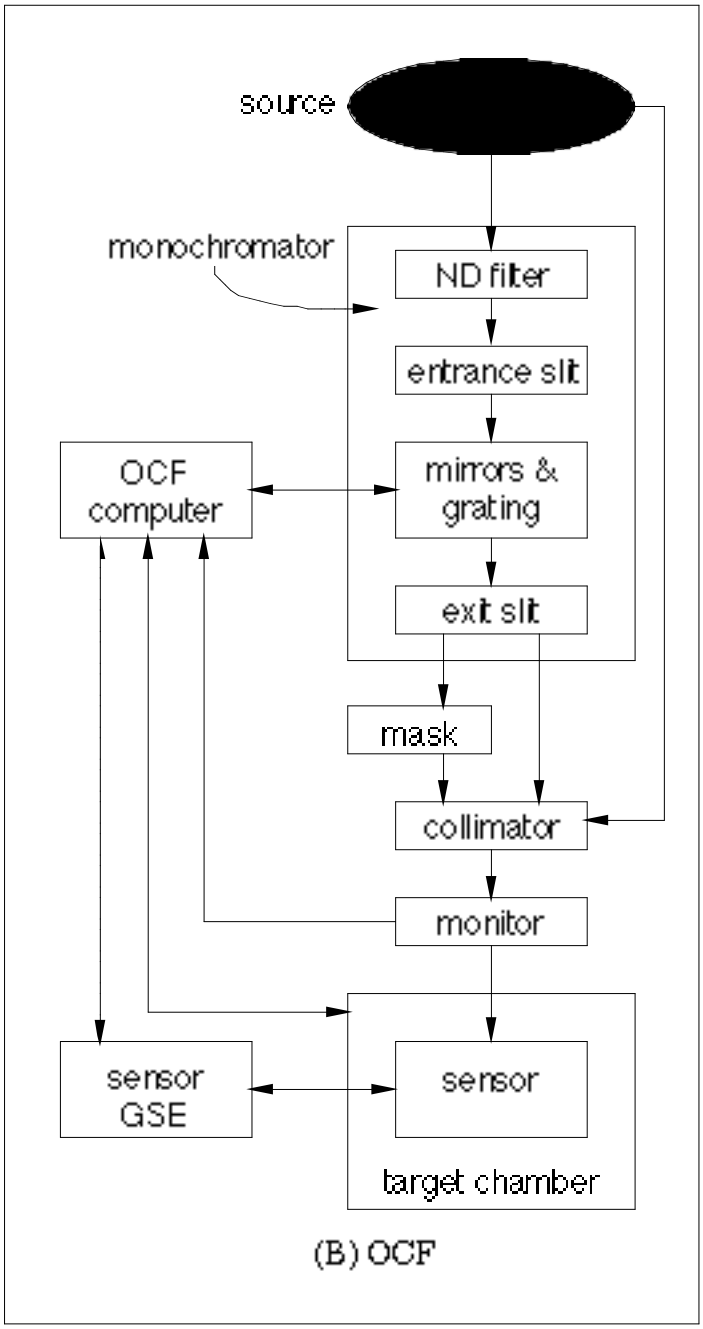

Figure 3. Schematic diagram of the OCF.

2.2. Optical Calibration Facility (OCF)

2.2.1. Overview

Figure 5 shows a schematic diagram of the OCF and identifies its various modules. A deuterium lamp with a MgF_2 window (Acton Model DS-775) provides a bright, stable source of FUV radiation which is wavelength-selected by the source monochromator (a f/6.9 0.5 m Czerny-Turner with a 1200 l/mm grating made by Acton Research). Wavelengths through the NIR are available with other sources through the same monochromator. The wavelength-selected light leaves the monochromator through a pinhole exit slit and enters a collimator which produces an 8 inch diameter beam. The instrument is mounted on a 3-axis (pitch, yaw, and horizontal translation) motion stage and observes this collimated light from the selected angle. Our reference detector, an EMR model 541G-09-17 photomultiplier with a MgF_2 window and a CsI photocathode, is mounted upstream of the instrument in an xy translation stage. This detector is calibrated with respect to a NIST standard CsTe photocathode vacuum photodiode. By moving a 1 mm aperture mounted in the reference detector stage in place of the reference detector and measuring the response of the instrument, we make a fiducial measurement of the position of the reference detector relative to the instrument aperture. The diameter of the active area of the detector is 0.375 inch. The detector is scanned across the aperture of the instrument in-between calibration measurements to accurately measure the monochromatic collimated irradiance of the beam.

Table 3 gives a summary of the features of the OCF. The vacuum system on the instrument side of the pinhole entrance slit of the collimator is entirely copper O-rings on conflat flanges, with Viton O-rings for the door and valves. The vacuum level of 6×10^{-7} torr is limited by the motion stages, which are lubricated with Braycoat, and also by the fact that flight instruments are regularly moved in and out from atmospheric pressure. The main background constituent, as measured by RGA, is water vapor. The GUVI instrument optics must meet a very strict molecular contamination limit of <A/10 (roughly a 1 nm equivalent thickness of contaminant),[8] which is monitored by a witness mirror periodically removed from the instrument. This level has been confirmed both by witness mirror FUV reflectivity testing and by a contamination certification test using a temperature-controlled quartz crystal microbalance (TQCM). The instrument may be moved in and out through a large door which covers the back of the chamber, and opens to a clean area. In addition, the motion stages sit on an optical bench on telescoping rails and may be rolled out of the chamber for easy access to the instrument. Another feature of the vacuum system is a thermal shroud which maintains a fixed temperature in a range from -35° C to 100° C. For GUVI, this allowed us to confirm that the line-of-sight at different scan mirror

angles was not affected by temperature. Control of the monochromator, motion stages, etc. and data collection is completely automated through a LabView system. We also have specified a standard network interface which allows the instrument GSE to collect data from the OCF computer regarding wavelength, motion stage positions, reference detector measurements, etc. These values are then merged with the instrument data.

Table 3. Summary of OCF as used for GUVI. Controlled by LabView program.

	Irradiance					**Beam diameter**	
Beam characteristics	127.5 nm	150 nm		180 nm			
	$8x10^8$ ph/cm^{2}s	$2x10^8$ ph/cm^{2}s		$4x10^7$ ph/cm^{2}s		200 mm	
	Operating collimation	**Operating resolution**		**Best resolution**		**Out-of-band light**	
Fine qualities	0.03°x0.01°	0.5 nm FWHM		0.03 nm FWHM		< 0.02%/nm @ 145 nm	
	Selectability	**Range**		**Filter wheels**			
Wavelength	Continuous	117.5-1100 nm		Density	Bandpass	Quartz, Pyrex, glass	
Bandpass filters used for GUVI	**Wavelength**	122 nm	132 nm	150 nm	152 nm	200 nm	240 nm
	FWHM	9 nm	17 nm	19 nm	68 nm	22 nm	22 nm
Light sources	deuterium	mercury		xenon		halogen	
	Type	**Grating**		**Operating entrance slit**		**Operating exit slit**	
Monochromator	0.5 m Czerny-Turner	1200/mm ruled blazed		0.25x10 mm		0.25x0.75 mm	
		Yaw		**Horizontal translation**		**Pitch**	
Motion stage	**Range**	-180° to +180°		-50 to +100 mm		-90° to +90°	
	Accuracy	0.01°		0.01°		0.01 mm	
	Pumping system	**Vacuum level**		**Minimum temp.**		**Maximum temp.**	
Vacuum/Thermal	3 cryopumps	$6x10^{-7}$ torr		-35° C		+100° C	
	Type	**Photocathode**		**Aperture diameter**		**Scanning**	
Reference detector	Photomultiplier	CsI/CsTe		9.5 mm		x-y in situ	

In Table 3, irradiance is given under GUVI operating resolution with no filters. We use neutral density filters to reduce the irradiance by 2-4 orders of magnitude, to a level appropriate for the instrument. Peak transmission of the narrowband filters is 10-40%. The collimation may be improved to a measured 0.008° by using a 150 μm diameter pinhole as a monochromator exit slit.[9] The wavelength range may be extended beyond 1100 nm by replacing the grating.

The GUVI instrument has a requirement of <0.024%/nm out-of-band response, and so out-of-band light is an important consideration in the calibration system. Narrow-band and quartz filters are used to measure the instrumental scattered light at levels <0.014%/nm. As shown in Table 3

	Irradiance					**Beam diameter**	
Beam characteristics	127.5 nm	150 nm		180 nm			
	8x108 ph/cm2s	2x108 ph/cm2s		4x107 ph/cm2s		200 mm	
	Operating collimation	**Operating resolution**		**Best resolution**		**Out-of-band light**	
Fine qualities	0.03°x0.01°	0.5 nm FWHM		0.03 nm FWHM		< 0.02%/nm @ 145 nm	
	Selectability	**Range**		**Filter wheels**			
Wavelength	Continuous	117.5-1100 nm		Density	Bandpass	Quartz, Pyrex, glass	
Bandpass filters used for GUVI	**Wavelength**	122 nm	132 nm	150 nm	152 nm	200 nm	240 nm
	FWHM	9 nm	17 nm	19 nm	68 nm	22 nm	22 nm
Light sources	deuterium	mercury		xenon		halogen	
	Type	**Grating**		**Operating entrance slit**		**Operating exit slit**	
Monochromator	0.5 m Czerny-Turner	1200/mm ruled blazed		0.25x10 mm		0.25x0.75 mm	
		Yaw		**Horizontal translation**		**Pitch**	
Motion stage	**Range**	-180° to +180°		-50 to +100 mm		-90° to +90°	
	Accuracy	0.01°		0.01°		0.01 mm	
	Pumping system	**Vacuum level**		**Minimum temp.**		**Maximum temp.**	
Vacuum/Thermal	3 cryopumps	6x10-7 torr		-35° C		+100° C	
	Type	**Photocathode**		**Aperture diameter**		**Scanning**	
Reference detector	Photomultiplier	CsI/CsTe		9.5 mm		x-y in situ	

, the calibration system has 0.02%/nm out-of-band light at 145 nm. Out-of-band values at other wavelengths depend on the spectral response function of instrument or reference detector. In particular, care must be taken to use additional filters at wavelengths >170 nm, because the instrument and the reference detector are both much more sensitive to the shorter wavelength light, so even minimal out-of-band light can cause a significant background signal. This is illustrated in Figure 4.

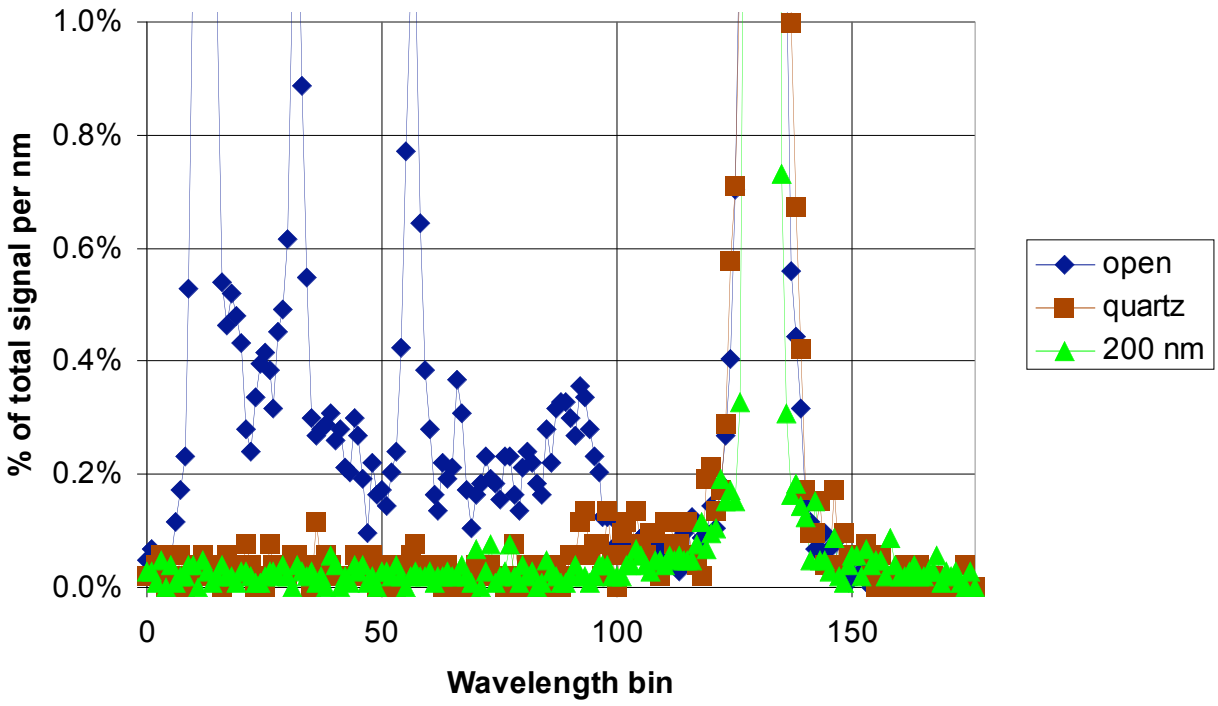

Figure 4. Instrument response to OCF light with a wavelength of 177.5 nm.

Figure 4 gives the response of the GUVI instrument to OCF light with the monochromator set at 177.5 nm. The peak on the right is the main line at 177.5 nm. With no filter, several other lines are visible out-of-band. In fact, the background rises as high as 2% of the total signal in a single out-of-band wavelength bin (5% per nm) at the tallest out-of-band peak. The use of a Suprasil quartz filter blocks light shorter than 160 nm and therefore allows one to characterize the instrument out-of-band scatter for background wavelength bins corresponding to wavelengths shorter than 160 nm. One can see the quartz cutoff at about wavelength bin 90. Below this wavelength, the scattering observed must be entirely in the instrument. The scatter can be reduced even more by using a 200 nm narrowband filter. Note the reduction of width of the main line is due to better focus, not reduced scatter. The 200 nm filter data set was taken after shimming of the detector to achieve final focus.

2.2.2. Monochromator

Figure 6 shows a schematic diagram of the OCF monochromator. The monochromator is of the Czerny-Turner type and has a focal length of 0.5 meters (f/6.9). Divergent light from a lamp source enters the monochromator chamber from one of two entrance slits. A diverter mirror

allows the selection of either of two possible sources that can be maintained on-line. From the diverter mirrors, the light travels to a parabolic mirror that focuses it onto a movable grating. The grating spectrally separates the light and reflects light of one particular wavelength to a second parabolic mirror. This second mirror focuses the light onto one of two exit slits. A second diverter mirror selects the desired exit slit. Typically, one exit slit contains a beam monitor while the other accepts the beam for output.

Special precautions ensure that light of the desired intensity will propagate to the exit slit. First, both the input and output slits include windows that attenuate light as little as possible. Second, the slits themselves may be changed to allow more or less light to propagate through the system. Third, a visible source typically inputs light through slit 2 and an ultraviolet source inputs light through slit 1; this arrangement ensures that the comparatively weaker UV beam need not undergo a reflection from the diverter mirror. Finally, all mirrors have an Al-MgF_2 coating (#1200) for optimum reflection, even in the far ultraviolet.

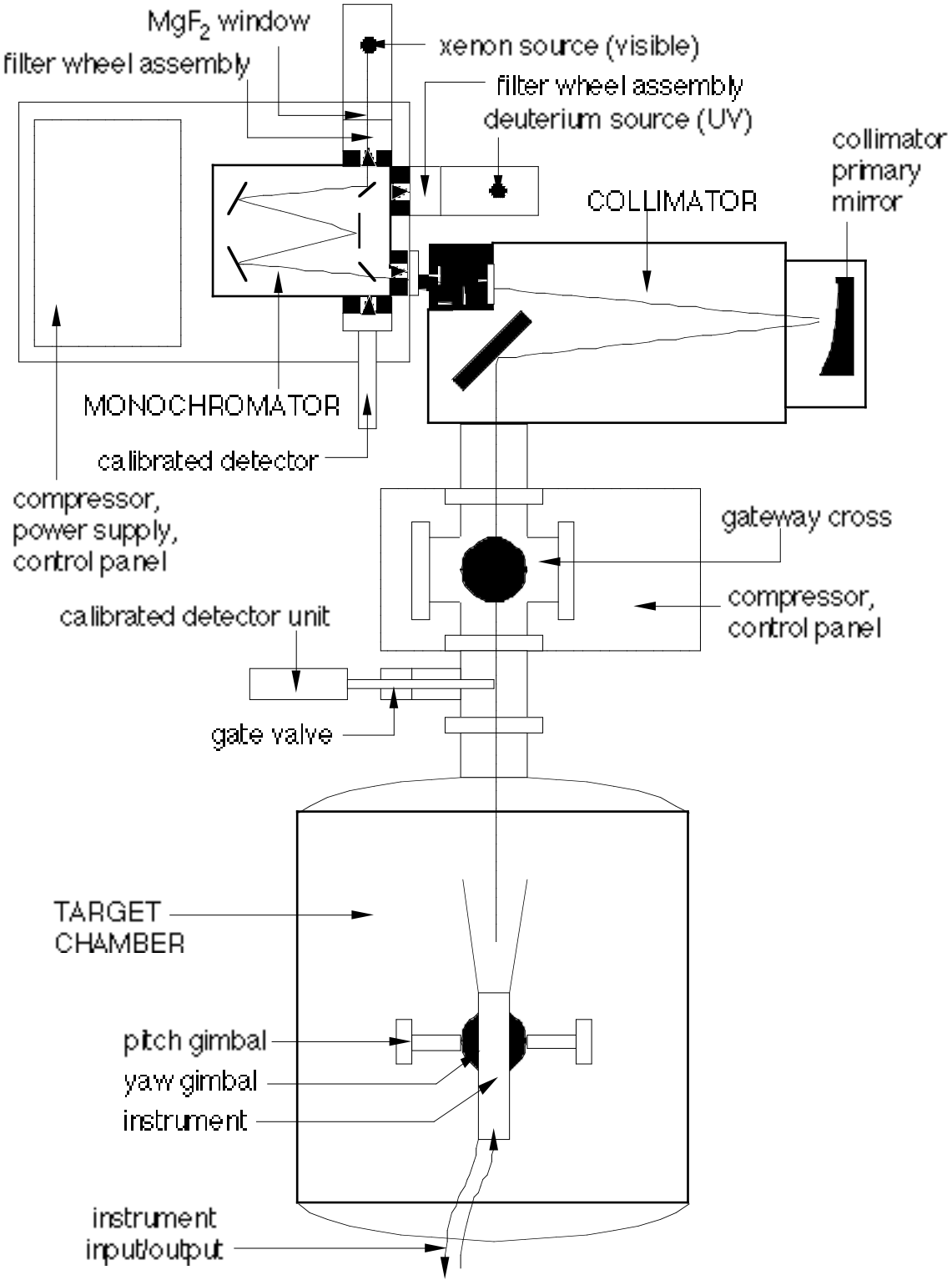

Figure 5. The Optical Calibration Facility (OCF).

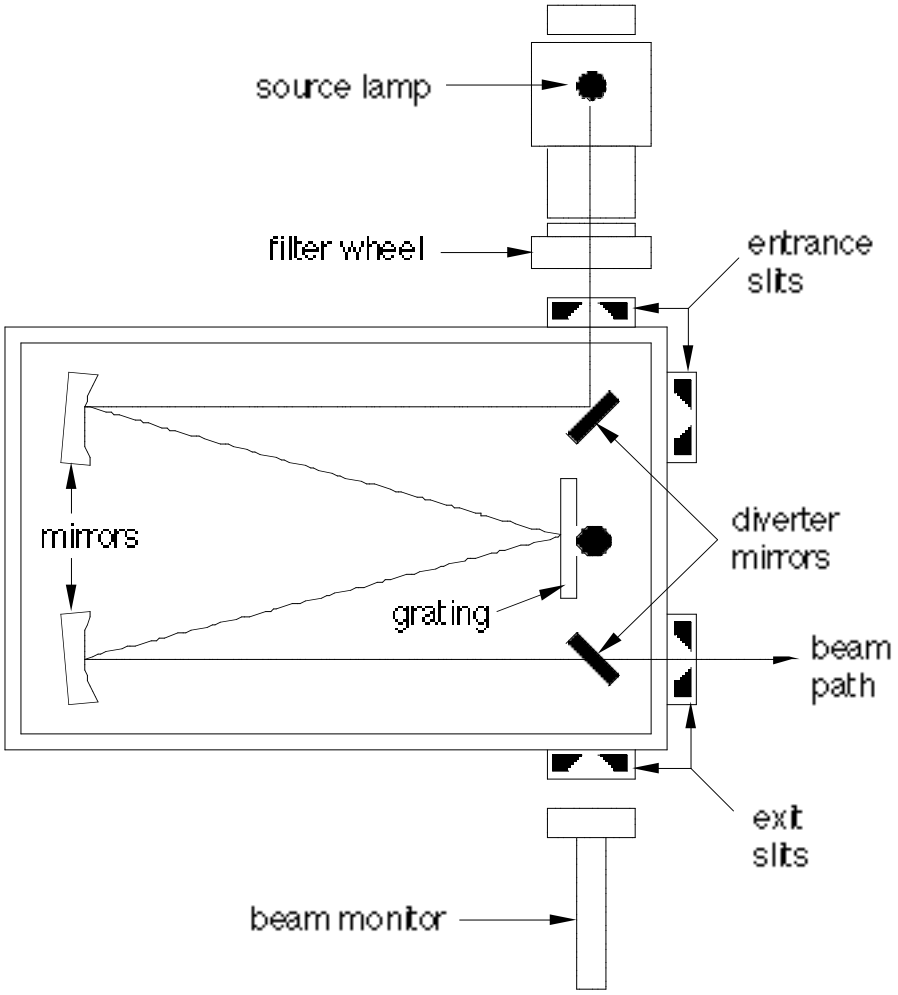

Figure 6. The OCF monochromator.

Interchangeable gratings permit the monochromator to output a wide range of wavelengths. Currently, the monochromator utilizes two flat gratings: one operates in the ultraviolet (~110-400 nm) and one operates in the near ultraviolet and visible (~300-900 nm). Table 4 summarizes the characteristics of these two gratings. The UV grating has a spectral resolution of ~0.22 Å at first order while the visible grating has a spectral resolution of ~0.24 Å. Furthermore, the visible grating is holographic. The monochromator has internal adjustments that allow the accurate selection of wavelength to the resolution of either grating.

Finally, the monochromator has adjustable entrance and exit slits. The slit height may be changed by moving two baffles along a graduated scale from a centerline fiducial. The slit width

may be changed by using a micrometer caliper mechanism. Adjustment of the slit height requires internal access to the slit housing, while adjustment of slit width can be done externally.

The monochromator and its slits and gratings were manufactured by Acton Research Corporation (ARC) or Acton, Massachusetts. ARC has provided full documentation of the characteristics and manufacturing history of its instrument.

Table 4. Monochromator Grating Characteristics

Grating/Groove designation	Blaze density	Blaze angle	Resolution wavelength	(1st order)
ultraviolet	1200 mm^{-1}	5.17°	150 nm	0.22 Å
visible	1201 mm^{-1}	8.63°	250 nm	0.24 Å

2.2.3. Collimator

The collimator accepts divergent rays from a point source and converts them into parallel rays. Essentially, this conversion represents the opposite function of an astronomical telescope. The use of middle and far ultraviolet radiation requires that the collimator employ all-reflecting optics. Figure 7 shows a schematic diagram of the OCF collimator.

The collimator employs two mirrors to parallelize the light and direct it through the exit port. Light first strikes a parabolic primary mirror, which has a diameter of 8 inches (20.32 cm) and a focal length of 56.35 inches (143.13 cm). The parallel rays strike a flat secondary mirror oriented at 45° to the parallel beam. Micrometer mounts secure both mirrors and allow the precise alignment of the input and output beams. (Because of the precision required, these adjustments consume most of the time required to set up the complete OCF for calibrations.) Both mirrors have a coating of $AlMgF_2$. This coating has an average reflectivity of 0.95% from ~250 nm to 750 nm. A stainless steel housing encloses the entire collimator and permits vacuum operation. The internal surfaces are coated with black chemglaze to reduce stray reflections.

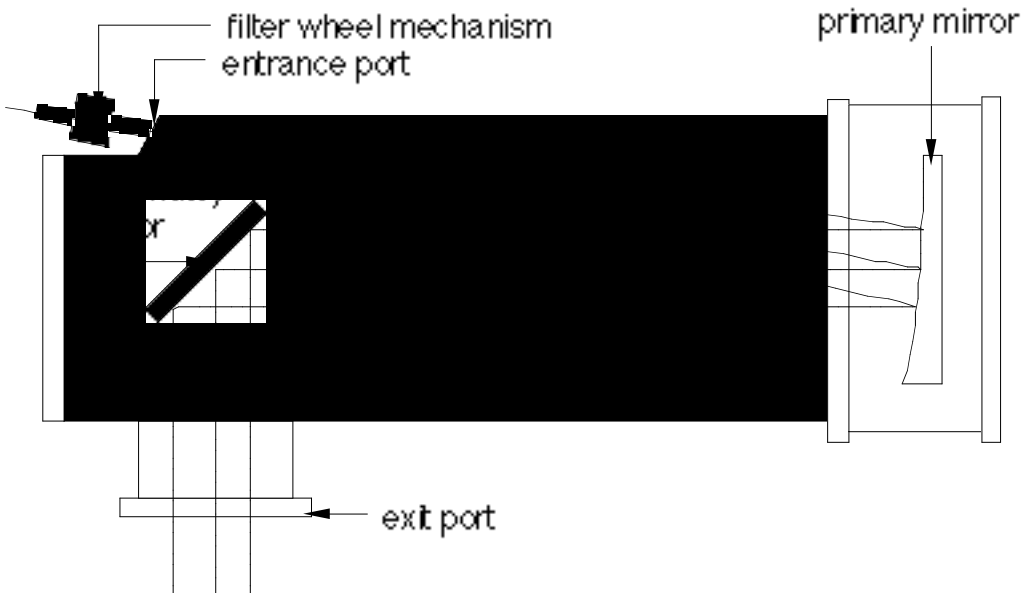

Figure 7. Detail of OCF collimator.

2.2.4. Target Chamber

The OCF target chamber consists of a large, spherical enclosure, various input and output ports, electrical connectors, and a dual-gimbal internal mount (see Figure 8). The present OCF enclosure measures 48 inches (1.23 m) in diameter and 60 inches (1.52 m) in length. The internal surfaces of the enclosure are coated with black chemglaze. The entire chamber rests on a movable framework. The usable internal diameter, including the thermal jacket, is approximately 44 inches.

Inside the enclosure, a target mounting table provides a stable platform to which the instrument is secured. This table has a two-axis gimbal that permits rotation in discrete steps of ~0.05°. The gimbals allow rotation of ±10° in yaw, and a range of 150° in pitch. In addition, two linear translation stages are being installed, which permit translation perpendicular to the optical axis in steps of ~1 μm. The translation stage has travel limits of ±5 cm. An external controller operates the rotation and translation of the mounting table.

Four feed-through connectors allow electrical access to the instrument during calibration in the chamber. These connectors may be interchanged to allow standard 25-pin connections.

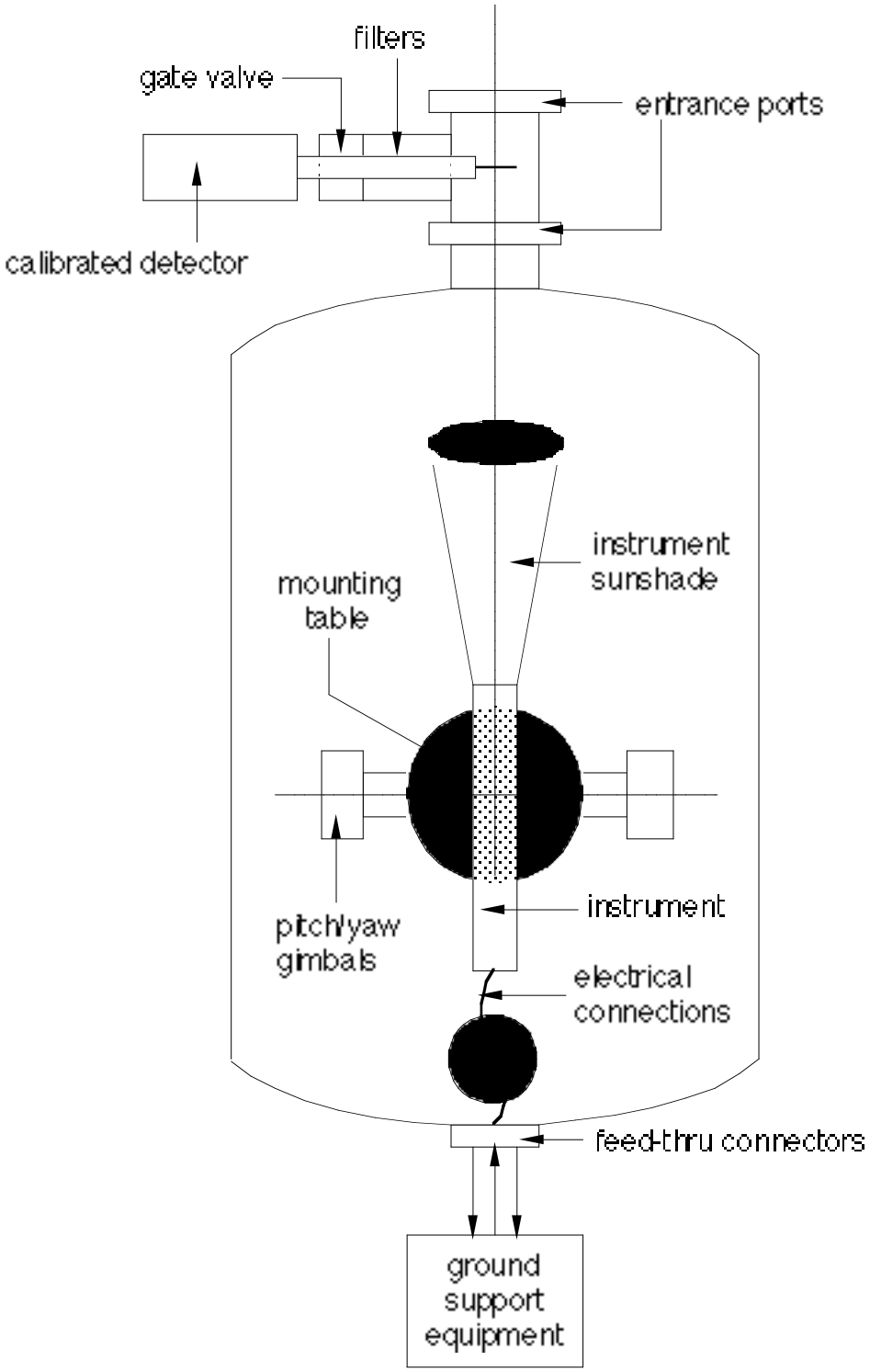

Figure 8. Detail of OCF target chamber.

2.2.5. Sources

The OCF used a deuterium lamp for the calibration of the GUVI instrument. The deuterium lamp provides ultraviolet radiation with wavelengths from 115 nm to 370 nm, with some emission lines below 165 nm. The lamp consists of a sealed tube filled with deuterium gas; the light escapes from the tube through an MgF_2 window. The emitting area (window) has a diameter of ~1 mm, which typically provides a beam divergence with f/10. The lamp provides a peak irradiance of $\sim 10^{13}$ photons/cm^2·s. The lamp consumes 15W of power and operates at 300mA and 70V.

2.2.6. Beam Monitors

An EMR 541G PMT measured the beam at the input to the target chamber for wavelengths ≤1700 Å. This detector has an MgF_2 window and a CsI photocathode. An EMR 541F PMT was used for wavelengths ≥1700 Å. Both detectors have been calibrated with respect to a NIST standard diode at the Homewood campus of JHU. The monitor package includes a bleeder string, preamplifier, amplifier, and discriminator. For all beam monitors, the beam irradiances are computed by converting detector counts to photon flux and folding in geometric factors such as area and solid angle.

2.2.7. Filters

The OCF will employ a number of filters. These filters serve to reduce the beam intensity and eliminate higher order spectra from the monochromator. A set of two filter wheels precedes each the entrance slit of the monochromator. Each filter wheel has seven positions. The first filter wheel contains neutral density filters (NDFs) ranging in attenuation strength from 1 to $\sim 10^{-4}$. The second filter wheel contains narrow-band filters to cut down on out-of-band light from the monochromator, so that out-of-band scatter In the Instrument may be accurately characterized. Filter transmission characteristics as a function of wavelength have been given by the manufacturer (ARC) and verified in-dependently by direct measurement in the OCF itself. The monochromator incorporates secondary filters at its output aperture to eliminate higher order spectral components. A four position filter wheel at the output slit contains three filters and one blank position. A Suprasil filter cuts off transmission (50% level) below 170 nm; a Pyrex filter cuts off transmission below 312 nm; a Schott glass filter cuts off transmission below 450 nm.

2.2.8. Use of GSE

The GUVI ground support equipment (GSE) will provide the means to test and monitor the instruments during ground calibrations, instrument and spacecraft check-out and will serve as a back-up during the mission. The GSE activities therefore include all activities relating to the sensor electronics units (SEUs), focal plane units, imager units, spectrographic imager units, and their integration with the digital control system (DCS) if GUVI. The GSE will test and monitor the sensor hardware in several different configurations. First, the GSE will monitor the detector by itself. In this mode, the GSE has direct control over the pulse width of the grating and voltage gains. Second, the GSE will directly control the spectrographic imager, exercising control of the various operating modes and also of the mechanical interfaces. Third, the GSE will control the SEU by simulating the interface. Fourth, the GSE operated in a "listen-only" mode in which the DCS controls sensor hardware. This mode simulates the operation of the entire instrument. Fifth, the GSE will function during spacecraft ground tests to monitor the behavior of the GUVI instrument. Sixth, the GSE will operate during the mission, accepting raw data from the mission control center.

3. SIS GROUND CALIBRATION

3.1. Introduction

Optical calibration, which is critical to reaching our error requirements, is difficult in the far-UV. All work must be done in ultrahigh vacuum, so in addition to the light being invisible, the optical components are inaccessible for adjustments during the measurements. In the visible and near-UV, blackbody sources are available which are bright and very stable. In contrast, far-UV sources such as plasma discharges are relatively weak and subject to aging and restrike errors. Often, only discrete wavelengths are available. Diffuse sources are difficult to make because of the low reflectivity of most surfaces in the far-UV. Because of these problems and others, even the standard detectors distributed by NIST are calibrated much less accurately than their counterparts in the near-UV and visible.[10]

Table 5 shows the GUVI error budget to reach our accuracy requirements for measurements of the environmental parameters. It was necessary to reach 8% accuracy in calibration. This would be easy in the visible, but it is difficult in the far-UV. Table 5 also shows a top-level breakdown of the most important calibration error budget terms. The largest item is the error in the NIST reference standard detector. Note that NIST actually quotes a 2σ error of 10%. The 5% figure

reflects the 1σ reporting used in this paper. Several improvements were made to the OCF for GUVI which reduced the uncertainty in the OCF beam flux by more than a factor of two. The beam uniformity was dramatically improved by the use of an ellipsoidal mirror in an off-axis configuration in the deuterium lamp. The other dramatic improvement was in the error contribution of changes in the beam over time. LabView automation allowed us to profile the beam in two dimensions before and after each individual data set. This completely eliminated errors due to long-term aging of the lamp, which is due to the formation of color centers in the MgF_2 window. It also eliminates restrike error, which is 5% for deuterium lamps.[11]

Table 5. Summary of GUVI error budget, with detail of calibration uncertainty.

Environmental parameters			**Calibration**			**OCF beam flux**	
Type of error	Amount		Type of error	Amount		Type of error	Amount
Brightness	8%		**OCF beam flux**	**6.5%**		NIST photodiode	5%
Pointing	6%		GUVI	3.5%		Transfer to ref. PM	3%
Calibration	**8%**		Radiance conversion	3%		Beam uniformity	2%
Inversion/theory	7%		OCF background	2%		PM count statistics	1%
Total	**15%**		**Total**	**8%**		**Total**	**6.5%**

In addition to the laboratory calibration discussed in this paper, the calibration plan for GUVI involves an on-orbit component, which has the same 8% error requirement as the laboratory calibration. As noted above, one of the main reasons FUV calibrations are less accurate than visible calibrations is the absence of a blackbody source which is bright enough in the FUV. If one only had a 40,000 Kelvin blackbody source in the laboratory, then these calibrations would be a lot easier. Well, in space one does have such sources. They are hot A and B dwarf stars. Their spectrum is close to blackbody at most wavelengths, and the spectrum is well characterized. In the FUV, the irradiance from these stars is stable, and known to 2-3% accuracy.[13,14] We use these stars as standard sources for our on-orbit calibration.

As discussed above and shown in Figure 6, our laboratory calibration uses the parallel light rays of collimated light. This is the same as our on-orbit calibration, since the stars are effectively point sources at infinity. We measure the response of the instrument to a given *irradiance* of collimated light. However, when we look at the airglow to measure environmental parameters, we see diffuse light from different directions filling our spectrometer slit. In order to measure

the airglow accurately and compute the environmental parameters, we require a *radiance* calibration.

Therefore, the laboratory calibration must satisfy two requirements: 1. We must be able to get a radiance calibration from the laboratory data, and 2. We must characterize the instrument well enough that we can convert an irradiance calibration to a radiance calibration on-orbit. The response of the instrument varies relatively little in the along-slit direction, and so an accurate conversion is not a problem for varying along-slit angle. However, the instrument sensitivity as a function of across-slit angle varies quickly, as does the shape of the response across the wavelength bins of the detector. To solve this problem, we measure the irradiance response at multiple closely-spaced across-slit angles in the laboratory. The sum of these datasets is the instrument response to a source that is diffuse in the across-slit direction, with a radiance that depends on the irradiance of the collimated light and the spacing of the across-slit angles. This gives a laboratory radiance calibration. Then, we can use the separate data sets for the different incoming angles to calculate the shape of the instrument response to a given stellar trajectory through the slit on-orbit. This will allow us to properly average the stellar calibration data and convert the stellar irradiance calibration to a radiance calibration. The laboratory calibration is vital both to validate the on-orbit calibration and to characterize the instrument sufficiently to perform the on-orbit calibration. The quantitative imaging of instrument response to collimated light at different along-slit angles is an ideal way to perform this characterization. The automation of the OCF and merging of OCF and GSE data were vital to handle the quantity of data necessary for this measurement.

The SIS will undergo three principal calibrations: spectral, radiometric, and geometric. Spectral calibration refers to the matching of spectral bin to optical wavelength. Radiometric calibration refers to the use of calibration tables and algorithms to convert instrument counts to irradiance (photons/cm^2·sec) or radiance (photons/cm^2·sec·sr). Radiometric calibration includes quantum efficiency as well as uniformity calibrations. Finally, geometric calibration refers to the alignment and positioning of the pixels within the FPU relative to the mirror scanning.

For extended sources, the radiance of pixel i,j is given by the conversion equation

$$L_{ij} = \frac{C_{ij} - D_{ij}(T)}{Q_{ij}\tau A\Omega} \qquad (1)$$

where A is the effective aperture area of the detector, W is the solid angle of a pixel, Q_{ij} is the quantum efficiency (counts/photon) of the whole instrument for a photon in spectral bin i and spatial bin j, and t is the accumulation time (seconds). C_{ij} represents the raw counts associated with pixel (i,j) and $D_{ij}(T)$ the instrument dark counts for pixel i,j as a function of temperature T. In designating a pixel, i refers to the spectral dimension ($0 \le i \le 176$), while j refers to the spatial dimension ($0 \le j \le 13$). The units of L_{ij} are photons / s cm^2 ster. To convert to units of Rayleighs, L_{ij} should be multiplied by $4\pi x10^{-6}$. To make conversion of counts to radiance easier the responsivity R_{ij} is defined.

$$R_{ij} = Q_{ij} A \Omega \qquad (2)$$

One may also define the irradiance response Q_{ij} A. The irradiance response is the number of counts/s the instrument produces from a given irradiance I in photons / s cm^2. The ground and on-orbit calibrations measure the irradiance response Q_{ij} A and the effective pixel field-of-view Ω. The results will be given in terms of responsivity R_{ij}. The value of τ is known on-orbit.

3.4. End-to-End Responsivity Calibration

Responsivity refers to the conversion of instrument counts to photons. In this formalism, "counts" refer to the digital counts recorded by the ground support equipment, which is presumably the same as the counts placed in the telemetry stream during the flight. Determination of responsivity represents the actual radiometric calibration of the instrument. Responsivity includes effects of photocathode quantum efficiency, window transmissivity, optical throughput, etc.

We have chosen a deuterium lamp-monochromator-collimator for the SIS calibration. We address the problem with the time of data collection by using 20 samples along the wavelength direction, rather than the full 176 wavelength bins. This gives 20 wavelengths x 14 pixels x 2 detectors = 560 data sets for a single scan mirror angle, a large but manageable number. We then measure scan mirror reflectivity at 20 wavelengths x 12 scan mirror angles x 3 pixels = 720 data sets. These measurements are made with the collimated beam focused inside the wide slit, so that the SIS acts as a slitless spectrometer. This is the irradiance calibration, giving the counts/s produced by the detector for a given irradiance from a point source at infinity. This is analogous to the on-orbit calibration using standard stars.

In order to use the irradiance calibration information to perform a radiance calibration, we must include the response as a function of viewing angle. The slit function of the instrument is simply the count rate as a function of angle observed as the instrument is rotated in the collimated beam, in such a way that the light is first blocked by one edge of the slit, then passes through the slit, and then is blocked by the other edge of the slit. The irradiance response is divided by the effective field-of-view calculated from the slit function and the pixel size (0.85°) to give the radiance responsivity.

The GUVI responsivity is shown in Figure 9 and Figure 10.

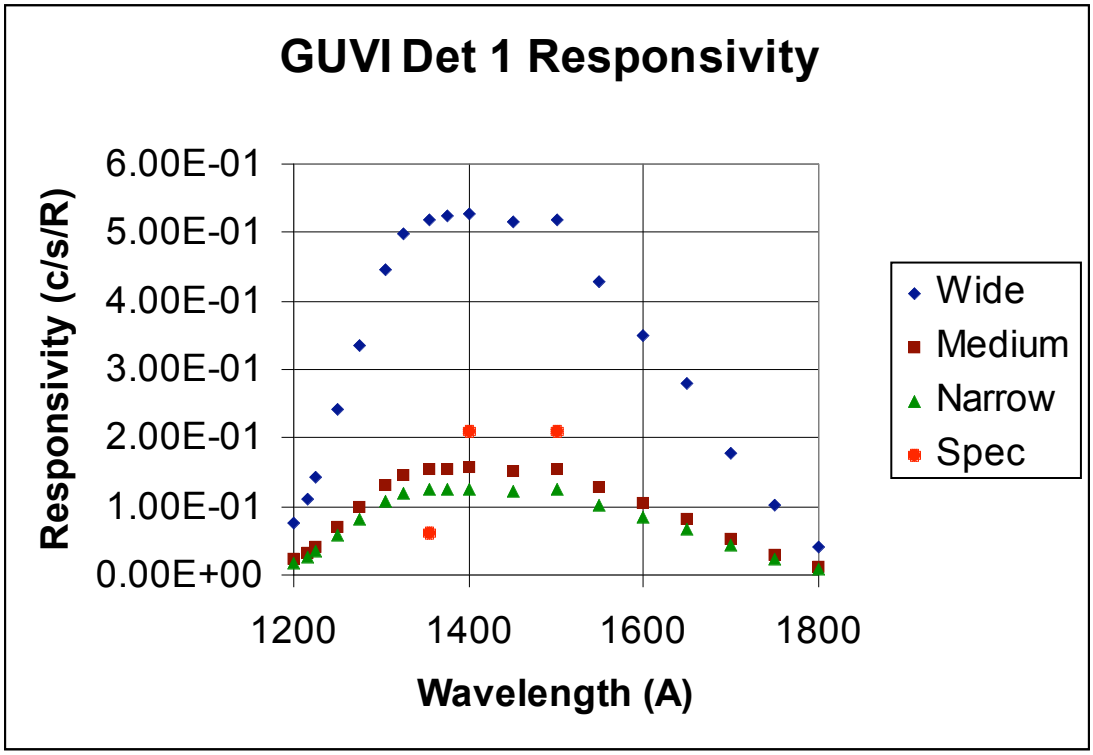

Figure 9. GUVI detector 1 responsivity.

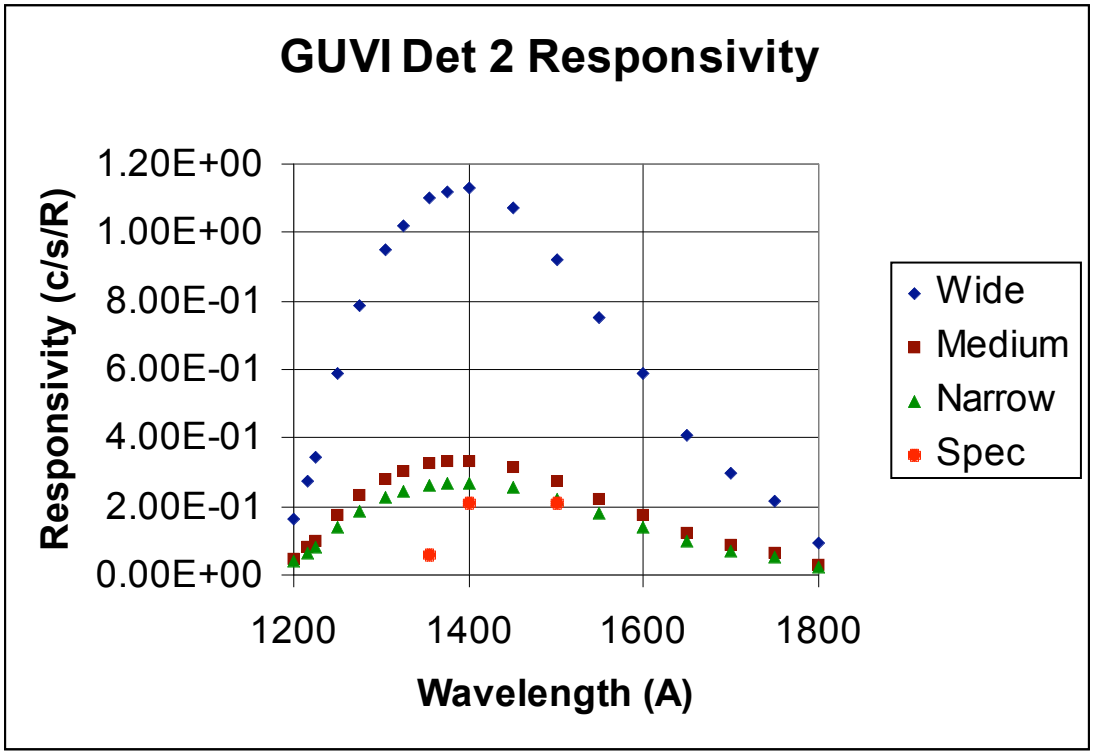

Figure 10. GUVI Detector 2 responsivity.

3.4.1. Reference Source Characterization

Our deuterium lamp-monochromator-collimator produces an 8-inch diameter collimated monochromatic beam. The portion of this beam which enters the aperture of the SIS is sampled by a reference detector mounted in front of the instrument. The reference detector is a model 541G-09-17 photomultiplier made by EMR Photoelectric, with a MgF_2 window and a CsI photocathode. The reference detector will be calibrated at the Homewood campus of Johns Hopkins University, using a NIST CsTe photodiode as a reference. The edges of our CsI photocathode are masked to give a 9.5 mm diameter, and both the NIST detector and the photomultiplier are underfilled by a 7.5x7.5 mm beam. The error in this calibration is estimated at 7%, 5% (1σ) due to error in the NIST reference, and 5% due to beam repeatability and photocathode nonuniformity. In addition, we plan to calibrate the photomultiplier against our own silicon NIST detector. By overfilling the detectors with a uniform input beam, and masking the NIST detector to the same 9.5 mm diameter as the photomultiplier, we will be able to reduce the transfer errors down to 3%. With the 5% error in the NIST detector, this will give a total uncertainty of 6%. It is not possible to use the NIST detector directly for instrument calibration, because it is a photodiode, and it is not sensitive enough to use at the small intensities the GUVI SIS is calibrated at. We can locate the NIST detector in the same part of the beam as our reference photomultiplier by using a mask with a hole in the photomultiplier mount.

In the near-UV, visible, and near-IR, current-stabilized incandescent lamps form a very stable and repeatable source of light. In the far-UV, the lamps involve some kind of discharge in a gas. The intensity produced by our deuterium lamp is repeatable only to about ±5% when turned off and back on again, and there are also drifts when the lamp is on. To minimize the error due to these effects, it is desirable to measure the beam with the reference detector as close in time as possible to the calibration of the instrument. We are able to correct for drift in the lamp intensity by scanning the reference detector in and out of the collimated beam in real time, allowing comparison of reference signal and SIS signal in the same collimated beam with a time delay of only a few minutes. This is sufficient to achieve 1% or less error due to drift in the reference lamp. The 9.5 mm diameter reference detector will measure the beam intensity in a 3x2 grid of positions chosen for best coverage of the 25x20 mm aperture of the GUVI SIS. Over this small grid, data collection will only take about 3 minutes per reference scan, including the time it takes for the reference detector to be scanned in and out. Given 560+720=1280 data sets as calculated above, and assuming a reference scan every 3 data sets (actually, for some data sets we will make a reference measurement every 7 data sets and still keep the 1% error

requirement), the reference scans will consume 21 hours and 20 minutes, or about 3 days of work time. This is actually faster than the 5 or 6 days used by the SSUSI beamscans, and fits well within our schedule.

3.4.2. Radiance Calibration

Our source provides a known irradiance I_l (phot/s) at each wavelength l. Assume the beam is focused to less than one spatial pixel and one wavelength bin of the sensor. Thus, all the energy I_l illuminates one and only one pixel. Denote the wavelength bin as i and the spatial pixel as j. Therefore, I_l can also be expressed as I_i. The wavelength is thus

$$\lambda = \lambda_i = A + B \cdot i \tag{29}$$

which comes from the wavelength calibration equation (16). One may write the irradiance (in photons/ s cm^2) as

$$I_\lambda = I_i = \frac{C_{ij} - D_{ij}(T)}{(Q_{ij}A)\tau} \tag{30}$$

where C_{ij} represents the raw counts, D_{ij} is the dark count, Q_{ij} A is the irradiance response (see Section 3.1 above), and τ is the accumulation time. This equation is similar to Equation 1 except the solid angle Ω is left out, because we are calculating irradiance rather than radiance. This expression can be rewritten to give the irradiance response Q_{ij} A.

$$Q_{ij}A = \frac{C_{ij} - D_{ij}(T)}{I_i \tau} \tag{31}$$

In (30) and (31), point spreading in both the spatial and spectral dimension may require C_{ij}-D to be determined by some sort of point source extraction technique. Then,

$$C_{ij} - D \rightarrow \Sigma\Sigma_{spot} C_{ij} - D_{avg} \tag{32}$$

where the sum runs over all points within the "spot" and D_{avg} is the mean background outside the spot, normalized to the number of pixels in the spot.

In order to convert the observed counts on-orbit to radiance, we need to know the radiance responsivity R_{ij}. Following Equation 2, $R_{ij} = (Q_{ij} A) \Omega$, where Ω is the solid angle of the field of view of one spatial pixel. Ω is calculated from the angular size of one spatial bin and from the slit function.

The angular size of one pixel is always 0.85° in the spatial direction. The SIS uses a wedge-and-strip detector, and calculates the coordinates of each detected photon from the W, S, and Z electrodes. The detected photons are then binned into pixels whose boundaries are defined in software. During initial optical calibration, the conversion from along-slit angle of the incoming beam to position on the detector is measured (see Section 3.5.4). Then, software is loaded to the flight processor to define the bins so that their angular size is 0.85°.

The contribution of the slit function to Ω is a bit more complicated. The slit function of the instrument is simply the count rate as a function of angle observed as the instrument is rotated in the collimated beam, in such a way that the light is first blocked by one edge of the slit, then passes through the slit, and then is blocked by the other edge of the slit. The slit function is independent of wavelength because the wavelengths are relatively short and the slits relatively large, so that geometrical optics dominates. Figure 11 shows the GUVI slit functions for the wide slit for different spatial bins.

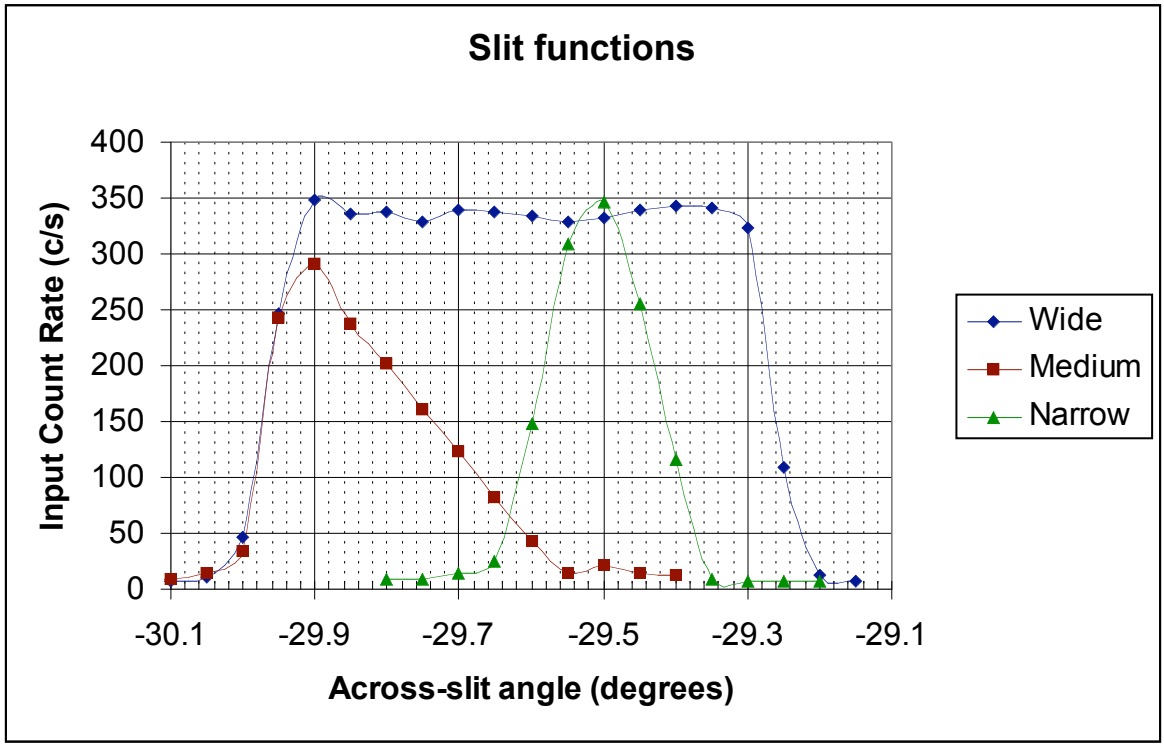

Figure 11. GUVI slit functions at central along-slit angle.

Equation 2 assumes that the slit function is rectangular, that (Q_{ij} A) is constant within the solid angle Ω, and Q_{ij} A = 0 outside Ω. As one can see from Figure 11, the signal actually drops off gradually across the slit. If the angle between the direction of propagation of the incoming collimated beam and a beam that would be focused at the center of the slit is defined as ψ, then Q_{ij} A = $Q_{ij}(\psi)$ A. In this case, Equation 2 must be generalized to

$$R_{ij} = \int Q_{ij}(\psi) A d\Omega \qquad (33)$$

In order to simplify the calculation, we write $Q_{ij}(\psi)$ A = Q_{ij0} A $Q_{\psi j}$. $Q_{\psi j}$ contains the part of the single-pixel irradiance response which changes with angle and with choice of slit (narrow, medium, or wide), and it is normalized so that Q_{ij0} A for any slit equals $Q_{ij}(\psi=0)$ A for the wide slit. SSUSI results have shown that within the 0.85° width of a single spatial bin the responsivity shows a negligible change. Therefore, within the 0.85° bin width, $Q_{\psi j}$ is just the slit function (such as one of the examples plotted in Figure 11, normalized to its value relative to the wide slit at ψ=0. Outside the 0.85° bin width, $Q_{\psi j}$ = 0.

Given the functional form of $Q_{\psi j}$, and the fact that it is nonzero in only a small range of solid angle, on the order of 1°x1°, we can rewrite Equation 33 as

$$R_{ij} = Q_{ij0} A(0.85^{\circ}) \int Q_{\psi j} d\psi \qquad (34)$$

We measure the slit function $Q_{\psi j}$, so we can easily compute the integral numerically. We define the effective slit width $\delta\psi_j = \int Q_{\psi j}\, d\psi$, and then the effective solid angle $\Omega_{effj} = (0.85°)\, \delta\psi_j$, so that $R_{ij} = (Q_{ij0}\, A)\, \Omega_{effj}$. $(Q_{ij0}\, A)$ is just the irradiance response measured at the center of the wide slit, and the equation for R_{ij} is the same as Equation 2 except the solid angle is replaced by an effective solid angle. Thus, by measuring the irradiance response for the wide slit at all wavelengths and spatial bins, and the slit function for each slit at one wavelength and all spatial bins, we can obtain an accurate value for the responsivity for all slits at all wavelengths and spatial bins.

For the measurements of the irradiance response with the wide slit, we use 20 samples along the wavelength direction, rather than the full 176 wavelength bins. This gives 20 wavelengths x 14 pixels x 2 detectors = 560 data sets for a single scan mirror angle, a large but manageable number. The time of integration of each measurement is chosen to give at least 2500 counts in the peak, so that the error due to counting statistics will be 2% at most.

3.4.3. Scan Mirror Reflectivity

All of the radiance responsivity data (Section 3.4.2 above) is taken with the scan mirror at nadir, which is defined as a 0° scan mirror angle. Of course, the reflectivity of the scan mirror will vary with angle, so the response of the instrument will vary with scan mirror angle. The biggest variation is a decrease in mirror reflectivity for near-grazing incidence rays in the short wavelength portion of the spectrum. This is for observations of the limb, which occur at maximum scan mirror view angle. The maximum angle of incidence of the rays is 77.2°, which happens at a +80° scan view angle. This decrease occurs because the rays must travel a greater path length through the MgF_2 coating of the scan mirror for grazing angles. The coating absorbs substantial light at the short wavelengths. There may also be a variation if the scan mirror coating is not perfectly uniform (or if nonuniform contamination is present), since different areas of the scan mirror are seen through the instrument aperture at different scan mirror angles and along-slit angles.

Therefore, we measure the responsivity of the instrument at different scan mirror angles, relative to its responsivity at nadir. We will use scan mirror angles of 80°, 76.8°, 73.6°, 70.4°, 60°, 45°, 30°, 15°, 0°, -20°, -40°, and -60°. For every scan mirror angle, the instrument must be rotated it so that the collimated beam is focused in the center of the slit to about ±0.05° accuracy in across-slit angle. The rotation necessary for the cradle holding the instrument cannot be calculated to such accuracy, so it is necessary to center the beam in the slit by taking counts as a function of across-slit angle. The measurements are made in the same way as the radiance responsivity measurements described in Section 3.4.2. The wide slit and the primary detector are used for all of them. We make measurements for all 20 wavelengths, and for along-slit angles of 0° and ±5.46°. This makes 20 wavelengths x 12 scan mirror angles x 3 pixels = 720 data sets.

We measured the scan mirror reflectivity at 3 along-slit angles because the area of the mirror seen by the instrument aperture changes as the along-slit angle changes. The extreme along-slit angles do not share any scan mirror area with each other, but each do share area with the 0° along-slit angle. Given a balance of time constraints and accuracy requirements, 3 along-slit angles seemed the optimal number or measurements.

The radiance responsivity described in Section 3.4.2 is simply multiplied by the reflectivity relative to 0° scan angle to give the overall responsivity of the instrument at each wavelength, scan angle, and along-slit angle.

3.4.4. Noise Background or Dark Count

Instrument noise background or dark count refers to the collective instrumental backgrounds within the photocathode, optics, electronics, etc. This background appears either as counts randomly scattered on the focal plane or as a constant count level. In the former case, the random counts cannot be subtracted simply because they cannot be predicted. In the latter case, however, adequate characterization of a constant count background may allow its subtraction.

The measurement of dark count relies on the simple relation

$$C_{ij} = C_{ij}^{source} - D \qquad (35)$$

where C_{ij} is the measured counts in pixel (i,j), C_{ij}^{source} are the counts arising from the scene (or the signal), and D is the dark counts arising from instrumental effects. The dark count D could may depend on temperature, detector voltage, etc.

The calibration proceeds by operating the SIS in total darkness. In this case, $C_{ij}^{source} = 0$, and the measured counts represents the dark count. The GSE merely records the count level over the entire detector array. The mean dark count can be determined by averaging over all pixels in the array namely,

$$D = \frac{1}{N_x N_y} \sum_i \sum_j C_{ij} \qquad (36)$$

Dark count measurements were performed during the other calibrations in the OCF.

3.5. Line fractions and spatial and spectral scatter

3.5.1. Introduction

End-to-end calibration refers to the calibration of the assembled SIS sensor, which consists of the flight detector, the flight optics, and the electronics. The end-to-end calibration will test the sensor under conditions as close as possible to those expected during flight. Most of the SIS calibration effort will concentrate on the end-to-end calibration.

3.5.2. Line fractions and color lookup tables

The line fractions are the normalized response of a single spatial pixel to a monochromatic diffuse source filling the slit. They were measured by summing the Images obtained as the collimated point source was scanned across the slit. These tables tell how much 1216, 1304, and 1356 Å radiation occurs in each spectral bin for each spatial bin. The line fraction tables were also used to generate the color lookup tables for the flight software. The color lookup tables define which wavelength bins are summed to generate each color at a given spatial pixel in imaging mode. For the 1216, 1304, and 1356 Å colors, wavelength bins with a line fraction value ≥ 10% of the peak line fraction value for the same spatial pixel are chosen. For the LBH I and LBH II colors, bins within the defined wavelength range (1400-1500 Å for LBH I, 1650-1800 Å for LBH II) are chosen.

3.5.3. Scattered light In the spectral direction

Scattering in the wavelength direction is very important, because the LBH 1 and LBH 2 colors cover a range of wavelengths, and hence integrate over the scattered light. They experience a background from the strong spectral lines at 121.6 nm and 130.4 nm. In addition, for disk observations there is a background from very strong Rayleigh scattering at wavelengths above 200 nm. In fact, the radiance from the disk is about 3 orders of magnitude higher for wavelengths above 200 nm than it is for in-band wavelengths 120-180 nm. This “red response” (actually response to UV of longer wavelength than in-band) was identified as a possible problem for the GUVI instrument, and a number of improvements were made to address it.

The red response was addressed in three ways: optical scattering, detector spectral response, and background subtraction software. As a risk reduction strategy, we set specifications in all three areas such that meeting the specification in any two would be sufficient to meet the science requirements. To control optical scattering, we procured a laminar ion-etched holographic grating from Carl Zeiss, Inc. This is an f/3 toroidal grating, and it was tested for efficiency and scatter in the vacuum ultraviolet by the manufacturer. In addition, the pop-up mirror used in conjunction with detector 2 was superpolished to bring its surface quality up to that in the rest of the optical train (see below). Scatter from the holographic grating was considerably better than our specification of 0.02%/nm, and no additional scatter was evident in detector 2 as compared with detector 1. Detector spectral response was the second red response issue. The CsI photocathode has a response that drops off very quickly at wavelengths longer than 180 nm.[15] However, CsI photocathode microchannel detectors show a response at these wavelengths which varies widely, so we put a specification on the maximum quantum efficiency as a function of wavelength. Detector 2 easily met this specification, but detector 1 was over by just a bit (see Table 6). The third approach to address red response was through background subtraction. Background pixels were established which measure the response of the instrument at indicated wavelengths shorter than 115 nm for 3 spatial pixels and 7 scan mirror angles. Because there is no actual signal at these wavelengths, due to the MgF_2 coatings and detector windows, these signals serve as reliable monitors of light scattered in the system. The scattering from 121.6 nm and 130.4 nm is accounted for by the measurements at those colors, and subtracted by individual scattering masks. The red response is then subtracted using a scattering mask multiplied by the remaining signal in the background pixels after 121.6 nm and 130.4 nm are accounted for. For detector 2, the calculated background due to red response is less than 1%, and the subtraction is unnecessary. For detector 1, it is less than 3%, and the uncertainty contribution from red response after background subtraction is less than 1%.

The scan mirror and telescope mirror of the GUVI instrument are superpolished to reduce scatter and eliminate crosstalk in the spatial channels. Generally, scatter increases as $1/\lambda^2$ at shorter wavelengths, making it difficult to fabricate low-BRDF optics in the FUV. However, scatter on-orbit is not as big an issue in the FUV as it is in the visible or IR. In the visible and IR, there is a dramatic increase in signal from the limb to the disk which is not present in the FUV. Figure 12
shows the count rate of the GUVI instrument for incoming light at large across-slit angles. The data are for the narrow slit and are normalized to a rate of one at slit center. The data as shown are equivalent to a scan mirror FUV BRDF of about 0.3 at 1° (with an equal BRDF for the

telescope mirror), which easily meets our specification. This is equivalent to an rms surface roughness of 0.37 nm over a 20x20 μm area of the optic. The spatial frequency bandwidth corresponding to this area is for scattering by more than 0.4°. Likewise, the surface roughness of the diffraction grating was measured to be 0.43 nm over a 30x30 μm range.

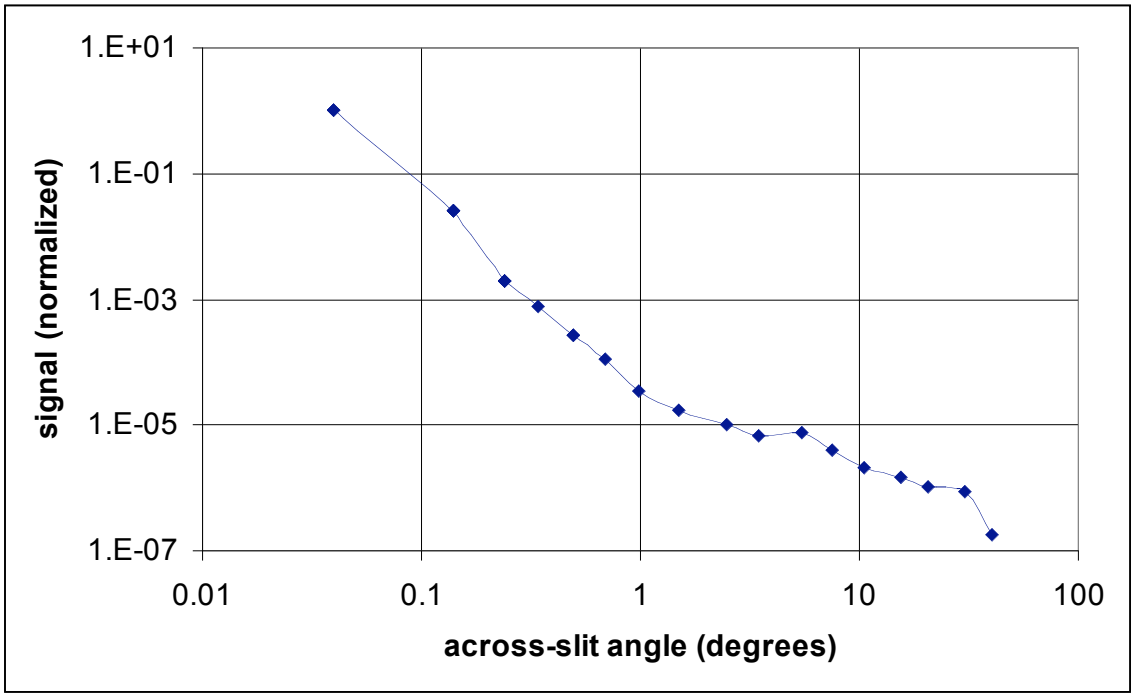

Figure 12. Off-axis scatter for GUVI with the narrow slit.

4. Conclusion

A summary of the measured performance of the GUVI instrument is given in Table 6. It satisfies all science requirements. The wavelength resolution with the narrow slit is a little over specification, but it is below for the medium and wide slits, and the science requirement that the 130.4 nm and 135.6 nm lines be resolved is easily met. Detector 1 has a red response which is slightly over specification, but, as discussed above, this generates an error of less than 1% in the final measured radiance. Detector 2 has a hot spot which brings its dark count slightly above the specification, but this will be excluded from the data by a careful choice of color tables, and will have no impact on the mission. A key element is calibration accuracy, which is satisfied.

Table 6. Summary of GUVI performance as measured.

	Specification	Performance
Wavelength range	1200-1800 Å	1175-1825 Å
Wavelength resolution	FWHM 1.3, 2.0, 4.2 nm	FWHM 1.6,1.9,4.0 nm
Field of View (across-slit)	FWHM 0.18°, 0.30°, 0.74°	FWHM 0.17°, 0.25°, 0.70°
Field of View (along-slit)	11.84° ± 5%	11.6°
Field of Regard	140°	139.8°
Scan step knowledge	0.05°	0.01°
Scan settling accuracy	0.05°	0.05°
End-end LOS pointing accuracy	0.1°	0.08°
Off-axis scatter	121.6 nm BRDF <= 0.5 @ 1°	121.6 nm BRDF 0.3 @ 1°
Wavelength scatter	<= 0.01% /wavelength bin	0.006%/wavelength bin
Detector red response	QE <= $5x10^{-4}$ @ 1950 Å	QE=$7.5x10^{-4}$,$1.5x10^{-4}$ @1950 Å
Maximum input count rate	300 kHz	600 kHz
Detector dark count rate	30 Hz	1 Hz, 40 Hz
Detector in-band QE	3% @1500 Å	3%, 11% @ 1500 Å
Overall instrument responsivity	0.06,0.21 c/s/R/pix @1356, 1450 Å	1: 0.35,0.38; 2: 0.25,0.21 c/s/R/pix
Calibration accuracy	8%	8%